Mobility Analysis of Nanocluster Formation and Growth from Titanium Tetraisopropoxide in a Flow Tube Reactor

Yuechen Qiao[1*], Li Li[1*], Justin Chen[1], Suo Yang[1], & Christopher J. Hogan Jr.[1**]

[1]Department of Mechanical Engineering, University of Minnesota, Minneapolis, MN, USA

Submitted to:

Journal of Aerosol Science

[*]Contributed equally to this manuscript
[**]To whom correspondence should be addressed: CJH: hogan108@umn.edu

Abstract

In an effort to understand the earliest stages of nanocluster growth in gas phase synthesis systems, we apply a flow tube reactor with a differential mobility analyzer-Faraday cage electrometer system to examine nanocluster formation and growth in the sub-3.0 nm mobility diameter range from the decomposition of titanium tetra-isopropoxide (TTIP) in air. Measured mobility distributions are inverted accounting for the DMA transfer function, tubing losses, and the charging efficiency, estimated from a non-steady state charge model within a bipolar ion source. Measurements reveal two types of species in spectra. First, we detect discrete (narrow) peaks falling in the 0.5 nm – 1.5 nm size range which appear at different locations for positive and negative measurement modes. Second, we observe a larger, broadly distributed peak, which is similar in intensity for both positive and negative modes after data inversion, and which increases in intensity (concentration) and peak diameter with increasing precursor flow rate, increasing reactor temperature, and increasing residence time. We conclude that the latter broad peak arises from growing nanoclusters in the reactor. The narrower, sub 1.5 nm peaks, are most likely attributable to specific reactive intermediates from the decomposition of TTIP. We find that increasing TTIP concentration, reactor temperature, or increasing residence time, which furthers the extent of nanocluster formation, leads to the depletion of the sub 1.5 nm ions. Because of the large step size in diameter between neighboring sub 1.5 nm peaks, we also find it is unlikely that these peaks arise from small TiO_2 clusters. Therefore, our measurements suggest that nanocluster growth from TTIP is facilitated by surface growth of reactive intermediates from TTIP decomposition, with reactive intermediates detectable via mobility analysis. Furthermore, while nanocluster formation and growth is clearly detected, measurements do not make clear that the nanoclusters are fully oxidized TiO_2 nanoclusters for the synthesis temperature range examined.

1. Introduction

The nucleation and growth of metal and metal oxide nanomaterials in the vapor phase in reactors including but not limited to flames (Meierhofer & Fritsching, 2021), flow tubes (Wergen *et al.*, 2019), spark discharge systems (Meuller *et al.*, 2012; Němec *et al.*, 2020), non-thermal plasmas (Kortshagen *et al.*, 2016; Mangolini, 2017) and laser vaporization sources (Kim *et al.*, 2017) enables continuous, scalable material production, typically with high purity in comparison to liquid phase approaches (Swihart, 2003; Schulz *et al.*, 2019; Meierhofer & Fritsching, 2021). While spark discharges and laser vaporization systems may make use of bulk metals as precursors, the remaining techniques in large part utilize organometallic precursors, which have modest-to-high vapor pressures at the synthesis temperature and pressure. Nanomaterials in these systems are presumably formed via the decomposition of the precursor into partially-oxidized intermediates (Wang, 2011; Lindberg *et al.*, 2019), which then react to form nanoclusters, i.e., metal, metal oxide, or partially-oxidized organometallic species whose physical diameters (if approximated as spheres) fall into the sub-nanometer or single nanometer range. Qualitatively, current understanding of these reactors is that the extent of nanomaterial formation and growth increases with increasing reactor temperature, residence time, and precursor concentration.

However, in nearly all gas phase organometallic precursor synthesis systems, the reaction steps leading to the formation of nanoclusters are not well understood. This appears to be predominantly because of difficulties in detecting both reactive intermediates and nanoclusters themselves, simultaneously. Only a handful of studies (Kumar *et al.*, 2014; Wang *et al.*, 2014; Carbone *et al.*, 2016; Tang *et al.*, 2017) have probed nanocluster formation in gas phase systems and been successful in detecting growing sub-nanometer and nanometer scale clusters. Detection in such studies is frequently carried out via mobility analysis or mobility analysis

coupled with mass spectrometry, and in a number of instances peaks in mobility spectra related to the presence and decomposition of organometallic precursors have been detected (Fang *et al.*, 2014; Wang *et al.*, 2015; Vazquez-Pufleau *et al.*, 2020), but simultaneous nanocluster formation and growth beyond one nanometer in characteristic diameter has only been observed in limited circumstances (Wang, et al., 2014).

The nanocluster formation and growth process is critical in gas phase systems, as it defines the lower size limit of nanomaterials which can be synthesized, and if there is an energy barrier of nanocluster formation (i.e. nucleation), then it can be the rate limiting step in nanomaterial production (Girshick, 1997). There is therefore continued interest in refining and utilizing measurement systems which can detect nanocluster formation and nanocluster growth in gas phase synthesis. In this work, we have constructed and utilized a flow tube reactor system coupled with a differential mobility analyzer (DMA)-Faraday cage electrometer system to detect growing nanoclusters from the decomposition of titanium tetra-isopropoxide (TTIP) in air; TTIP decomposition is an established, scalable route for the production of TiO_2 nanoparticles (Jiang *et al.*, 2007), hence the earliest steps of nanoparticle formation are of interest. Measurements permit the detection of both negatively and positively charged ions and nanoclusters in the effective diameter range of 0.5 nm – 3.0 nm. The subsequent sections describe the measurement system in detail, including data inversion procedures accounting for charging efficiencies prior to mobility analysis, followed by presentation of both raw data and inverted size distributions. We demonstrate that both reactive intermediates and growing nanoclusters can be detected, with depletion of the mobility peaks attributed to reactive intermediates corresponding to further growth of nanoclusters.

2. Experimental Methods

2.1. Differential Mobility Analysis Measurements

A schematic diagram of the nanocluster formation and measurement system is provided in Figure 1. The system is similar to that used by Wang et al (2015), but is operated at higher volumetric flow rates. Titanium (IV) isopropoxide (TTIP, 97%, Sigma-Aldrich, Saint Louis, MO, USA) was placed inside of a mineral oil bubbler (Chemglass, Vineland, NJ, USA) at room temperature, and vaporized through the bubbler as a precursor to synthesize nanoclusters. The precursor concentration was controlled by a nitrogen (N_2) flow going through the bubbler at a rate of 23-68.5 sccm (standard cubic centimeters per minute). The TTIP vapor-saturated N_2 flow (with a nominal vapor pressure of 0.15 Torr, (Siefering & Griffin, 1990)) exiting the bubbler was diluted with 10 L min^{-1} of filtered air. To further vary the residence time in the furnace aerosol reactor without requiring a higher flow rate mass flow controller and without mixing a larger flow rate with the TTIP laden flow directly, a recirculating pump (model 48114_00, AMETEK Inc., Berwyn, PA, USA) was utilized with HEPA (high efficiency particulate air) filters to supply an extra 0-15 L min^{-1} of dilution air entering at the inlet of the furnace reactor; this flow was also pulled from the outlet of the furnace reactor when utilized. The recirculating flow rate was controlled by a needle valve and monitored by a mass flow meter (Model 4140, TSI Inc., Shoreview, MN, USA). The flow rates of N_2 and dilution air applied for all experiments reported are listed in Table S1 of the supporting information. After combining the TTIP-laden N_2, the dilution air, and the recirculating flow, the resulting gas mixture was directed into a nonporous alumina ceramic tube (Inner Diameter: 9.5mm; Length: 609.6 mm), placed inside of a tube furnace (Lindberg Blue Model: 55035A). The furnace was operated at nominal temperature settings of 350^o C, 475^o C, and 600^o C, also listed in table S1 for each experiment. The

temperature profile along the centerline of the flow within the furnace was measured by a type K thermocouple for all examined temperature-setting flow rate combinations, at 2.54 cm axial distance increments. 27 total measurements were made along the tube, and the temperature for each measurement point was recorded after the reading of the thermocouple reached a steady state. The temperature profiles are provided in Figure 2. As evidenced in the figure, peak temperatures were found to be above the nominal value set point for all conditions where the total flow rate was near 10 L min^{-1} (i.e. without the recirculating flow rate). Therefore, while we refer to furnace settings via their nominal temperatures, the furnace reactor had a temperature profile under all conditions varying more than 100^{o} C as the flow traversed the furnace. The furnace served to drive decomposition of TTIP, and the chemical nucleation of TiO_2 nanoclusters. We note that the temperature ranged examined in this study is in a much lower range than that where TTIP decomposition kinetics have been examined theoretically (Buerger *et al.*, 2015; Buerger *et al.*, 2017). Temperature measurements were performed to a location where the flow passed through a counter-current water jacketed heat exchanger. The heat exchanger had an inner tubing (304 Stainless Steel, ID: 2.88 mm, Length: 304.8 mm) and an outer tubing (304 Stainless Steel, ID: 11.45 mm, Length 304.8 mm) that are separated by spacers (Polytetrafluoroethylene (PTFE)). Within the heat exchanger, the flow temperature was near 0^{o}C because of the high flow of recirculating water from a recirculating, temperature controlled (at 0^{o}C) chiller (Model 6105PE, PolyScience, Niles, IL, USA). The heat exchanger served to quench gas phase reactions of TTIP and gas-phase intermediates, though does not cease the nanocluster growth process as nanoclusters may still coagulate (Ouyang *et al.*, 2012; Sharma *et al.*, 2019) and possibly grow by uptake of remaining reactive intermediates (condensation/surface growth). Furthermore, the heat exchanger ensured that the flow was not at

an elevated temperature before passing through the bipolar ionizer, which was a tube housing Po-210 source (0.5 mCi, NRD LLC, Grand Island, NY, USA). Also, evidenced in Figure 2, at distance of 60 cm downstream in the reactor, the temperature increases; this coincides with the presence of a metal fitting which was radioactively heated via the tube furnace heating elements.

In all experiments, 10 L min^{-1} of sample flow was passed through a Po-210 source (0.166 mCi at the time measurements were performed). The Po-210 source was used to impart a bipolar charge distribution onto nanoclusters and facilitate size distribution analysis via electrical mobility measurements (Wiedensohler, 1988; Gopalakrishnan *et al.*, 2015; Maißer *et al.*, 2015). After exiting the bipolar charger, the nanocluster-laden flow passed into a custom-made half-mini DMA (Fernández de la Mora & Kozlowski, 2013; Wang, et al., 2014) whose voltage was stepped in the 5-800 V range with a recirculating sheath flow (blower Model 497.3.267-17, DOMEL, Železniki, Slovenia), in order to obtain mobility spectra for the nucleated and grown nanoclusters. Because nanoclusters were largely below 2 nm in size (below the cut-off size of most condensation particle counters), nanoclusters transmitted through the DMA were sent into a Faraday cage electrometer (Model 642, Keithley Instruments, Cleveland, OH) and the current was used to infer the number concentration of charged nanoclusters transmitted for each applied DMA voltage (calculated as $\frac{I}{Qe}$, where I is the current measured by the electrometer, Q is the aerosol sampling flow rate going through the electrometer, and e is the electron charge of $1.602 * 10^{-19} C$). The DMA voltage was stepped in 26.5 V increments and measurements were stabilized for 5 s at each voltage (from 5 V to 800 V). For each measurement condition, three mobility spectra were collected and averaged for subsequent processing. Both negatively- and positively-charged nanocluster mobility spectra were collected with the DMA-electrometer combination, though in separate experiments. While efforts were made to have precisely equal

TTIP bubbler flow rates for positive and negative mode spectra, changing liquid levels in the bubbler frequently led to drift of this flow rate and the need to constantly tune it, hence these flow rates would slightly vary from one another. DMA calibration was carried out under all measurement conditions using an electrospray of methanol with several millimolar (nominally) of dissolved tetra-heptyl ammonium bromide (THAB, 99.6% titration, Chem-Impex International, Wood Dale, IL, USA). The electrospray was a custom-made source using a sharpened-tip silicon capillary (ID: 40um, Polymicro Technologies, Phoenix, AZ, USA) with 3 kV applied to the liquid by a metallic wire submerged into the THAB solution. The tetra-heptyl ammonium (THA^+) ions generated yielded the spectra displayed in Figure S1, and used to convert applied voltage to mobility using the published mobility for THA^+ ions (Ude & de la Mora, 2005). Calibration with the THA^+ was also used to determine the DMA sheath flow rate, as described in the supporting information.

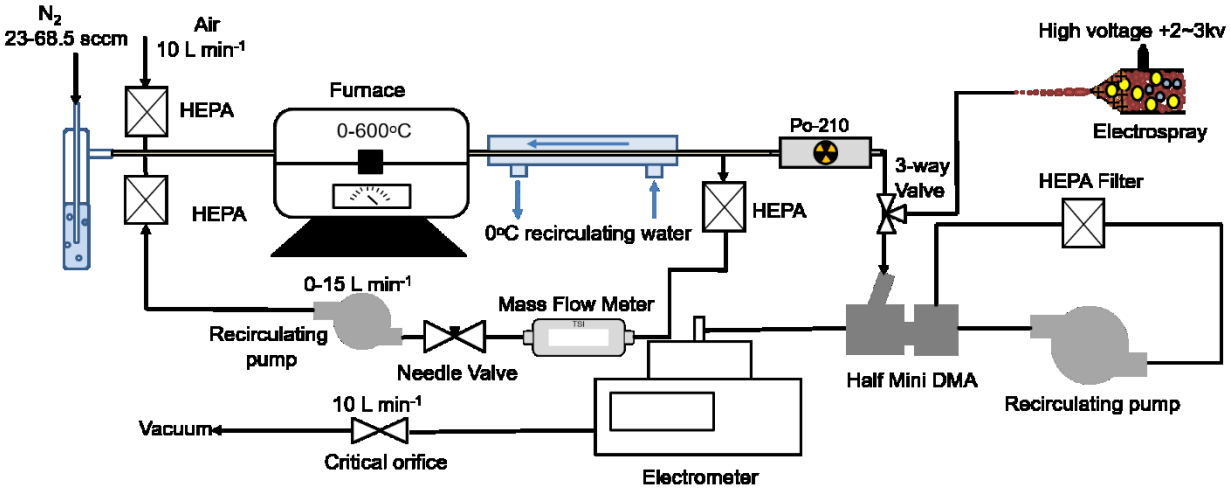

Figure 1. A schematic diagram of the TiO_2 nanocluster formation and measurement system, wherein TTIP vapor is passed into a furnace aerosol reactor and a DMA-electrometer combination is used to examine nanocluster mobility distributions.

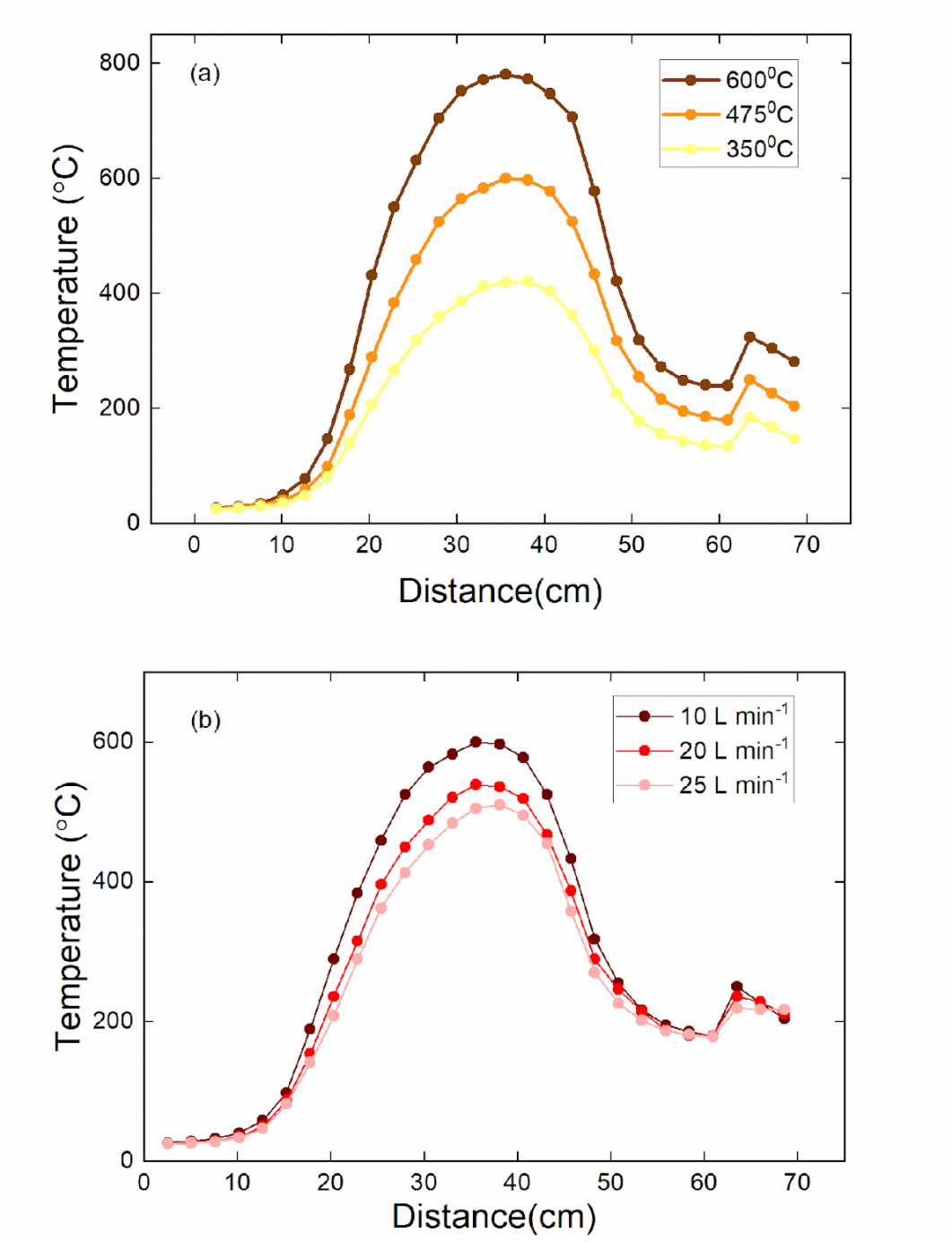

Figure 2. Centerline temperature profiles within the furnace aerosol reactor. Zero distance corresponds to beginning of the ceramic tube, which was outside the furnace. The labelled temperatures correspond to nominal set point temperatures on the furnace **(a)** without the application of recirculating flow, and **(b)** with application of recirculating flow, when a nominal temperature of 475° C was utilized, with the total flow rate through the furnace provided in the legend.

2.2. Charge Distribution Modeling and Data Inversion

The goal of DMA measurements was to determine the mobility based size distribution function for the formed nanoclusters. While standard methods are well-developed using DMAs for this purpose, particular care is needed inverting DMA measurements of nanoclusters (Kangasluoma *et al.*, 2020). First, in the current system, a sample flow rate of 10 L min^{-1} passes through a bipolar ionizer; such ionizers are conventionally utilized near 1 L min^{-1} or less. As the purpose of bipolar ionization in mobility measurement is to bring particles (or nanoclusters) to a known charge distribution (usually assumed to be a steady-state distribution), here we examine the charge distribution *a priori* in order to apply it in data inversion.

We solve a system of differential equations describing the evolution of the number concentration (n_p) of nanoclusters (of a specific diameter d_m, assumed equal to the mobility diameter, defined subsequently) of a specific charge state (p) (Marlow & Brock, 1975):

$$\frac{dn_0}{dt} = \beta_{-1}^{+} n_{-1} N_i^{+} + \beta_{+1}^{-} n_{+1} N_i^{-} - \beta_0^{+} n_0 N_i^{+} - \beta_0^{-} n_0 N_i^{-} \quad (1a)$$

$$\frac{dn_p}{dt} = \beta_{p-1}^{+} n_{p-1} N_i^{+} + \beta_{p+1}^{-} n_{p+1} N_i^{-} - \beta_p^{+} n_p N_i^{+} - \beta_p^{-} n_p N_i^{-} \quad (1b)$$

In equation (1a-b), $\beta_p^{\pm}$ is the collision kernel between a nanocluster of charge state p and of ion of $\pm$ polarity (Fuchs, 1963), N_i is the ion concentration. We restrict our scope to diameters below 3 nm in solving this system of equations. In this case, particles exiting the DMA are singly charged, and equation (1b) can be simplified by neglecting doubly charged terms:

$$\frac{dn_0}{dt} = \beta_{-1}^{+} n_{-1} N_i^{+} + \beta_{+1}^{-} n_{+1} N_i^{-} - \beta_0^{+} n_0 N_i^{+} - \beta_0^{-} n_0 N_i^{-} \quad (2a)$$

$$\frac{dn_{+1}}{dt} = \beta_0^{+} n_0 N_i^{+} - \beta_1^{-} n_1 N_i^{-} \quad (2b)$$

$$\frac{dn_{-1}}{dt} = \beta_0^{-} n_0 N_i^{-} - \beta_{-1}^{+} n_{-1} N_i^{+} \quad (2c)$$

We assume the concentration of both positive and negative ions are equivalent, and based upon measurements (presented in the *Results & Discussion* section) we estimate $N_i^- = N_i^+ = 4.81 \text{ x } 10^{10}\ m^{-3}$. For the collision kernel, $\beta_p^{\pm}$, we apply the models of Li et al (Li *et al.*, 2020; Li & Gopalakrishnan, 2021; Suresh *et al.*, 2021) which are an extension of the charging model of Gopalakrishnan et al (2013) to include unlike charged nanocluster-ion collisions. We remark that these collision kernels have recently been shown to yield steady charge distributions in better agreement with measurements for nanoparticles (Li, et al., 2020; Husmann *et al.*, 2021; Suresh, et al., 2021) than the commonly employed Happel & Frick (1986) modification to Fuch's (1963) limiting sphere theory, which was used in developing Wiedensohler's (1988) regression expression for calculating the steady-state charge distribution of nanoparticles during bipolar ionization. Details on the functional form of the collision kernels utilized are provided in the supporting information. The peak values of electrical mobilities (Z_i) for positive and negative ions were measured using the DMA by passing air through the bipolar ionizer to be $Z_i^+ = 1.43\ cm^2V^{-1}s^{-1}$ and $Z_i^- = 1.88\ cm^2V^{-1}s^{-1}$ (also presented in the *Results & Discussion* section). For collision kernel calculations, we approximated the ion masses (m_i) using the mobility-mass regression of Mäkelä et al. (1996):

$$Z_i = \exp\left[-0.0347\left(ln(m_i)\right)^2 - 0.0376ln(m_i) + 1.4662\right] \quad (3)$$

m_i is the ion mass in Da and Z_i is input in $cm^2V^{-1}s^{-1}$. At the same time, we remark that there is not a singular relationship between mass and mobility for ions generated by bipolar ionization sources in air (Maißer, et al., 2015), as the mobility is dependent upon the ion structure and its interaction with surrounding air molecules (Larriba & Hogan, 2013b; Larriba-Andaluz & Carbone, 2021), and not strictly the ion mass. The lack of independent mass measurements for mobility-identified ions hence introduces some ambiguity into calculations.

Following the conversion from DMA set voltages to particle mobilities Z_m, we infer peak transmitted mobility diameter d_m using the equations (Larriba & Hogan, 2013a; Larriba-Andaluz & Carbone, 2021):

$$\frac{1}{Z_m} = \frac{4\rho_{gas} c_{red} \Omega}{3e} \tag{4a}$$

$$\Omega = \frac{1.36\pi}{4}\left(d_m + d_g\right)^2 \xi \tag{4b}$$

$$c_{red} = \sqrt{\frac{8k_b T}{\pi m_{red}}} \tag{4c}$$

In equations (4a-c), Ω is the collision cross section, ρ_{gas} is the gas mass density, c_{red} is the mean thermal speed of the reduced mass (m_{red}, assumed equivalent to 29 Da), k_b is Boltzmann's constant, T is the temperature, d_g is the effective gas molecule diameter (assumed to be 0.3 nm), e is the unit electron charge, and ξ is a correction factor to account for the effect of the ion-induced dipole potential on the drag force on nanoclusters (Fernández-García & Fernández de la Mora, 2013). For simplicity $\xi = 1$ is assumed in conversion of Z_m to d_m.

While equations (4a-4c) enable estimation of the mobility diameter for nanoclusters transmitted through the DMA for each applied voltage (yielding nanocluster concentration for each applied voltage), we also make effort to account for the DMA transfer function width in converting concentration measurements to size distribution functions. To do so, the DMA transfer function, θ_{DMA}, is approximated as triangular (neglecting diffusion, (Stolzenburg & McMurry, 2008)) with a FWHM (full width at half maximum) of 1/10.8, based upon the ratio of the aerosol flow rate to sheath flow rate (Knutson & Whitby, 1975). This ratio was determined as described in the supporting information using the DMA dimensions from Wang et al (2014). Using equations (4a-c) to link mobility diameter to electrical mobility, we define upper (d_u) and lower limit (d_l) mobility diameters for each DMA voltage applied. Then, with the inferred

nanocluster concentration for each DMA setting ($N(d_m)$), the transfer function, and the charge fraction ($f_p(d_m)$, where $p = \pm 1$, determined via equations (2a-c)), the nanocluster size distribution function is estimated as:

$$\frac{dN}{dln(d_m)} = \frac{N(V_i, d_m)}{\theta_t(d_m) f_p(d_m) \int_{ln(d_l)}^{ln(d_u)} \theta_{DMA} dln(d_m)} \quad (5)$$

In equation (5), $\theta_t(d_m)$ is the penetration of nanoclusters of the selected mobility diameter through the system tubing, from the furnace outlet to the DMA inlet. This was calculated as described in the supporting information (Figure S2) using classical diffusion-convection mass transfer relationships for both laminar (Gormley & Kennedy, 1948) and turbulent flows (Dittus & Boelter, 1985). While approximate, we remark that charge correction and DMA transfer function influences have only been accounted for in several prior studies (Wang, et al., 2014; Carbone, et al., 2016; Tang, et al., 2017) wherein high sheath flow rate DMAs (often termed "high resolution DMAs") were used examine nanocluster formation in high temperature (Fang, et al., 2014; Vazquez-Pufleau, et al., 2020; Sharma *et al.*, 2021) and non-thermal plasma reactors (Kumar, et al., 2014). Furthermore, to our knowledge, no prior efforts have dealt explicitly with the non-steady state nature of the charge distribution (though efforts to do so are found in (Carbone, et al., 2016)), resulting from high transport flow rates needed for nanocluster measurements.

3. Results & Discussion

In total, measurements yield positively and negatively charged nanocluster concentrations as well as ion concentrations for variable furnace temperature settings, TTIP injection rates, and system residence times. We first discuss the charge distribution calculations needed to apply

equation (5) to invert size distributions from concentrations, followed by presentation of raw concentration results, and finally, inverted size distributions.

3.1. Nanocluster Charge Distribution

The charge distribution on nanoclusters passing through the bipolar charger is dependent on nanocluster diameter, the residence time within the charger, ion properties, including mobility and mass, as well as ion concentrations relative to nanocluster concentrations (Adachi *et al.*, 1985). The mobility diameter distributions and inverse square root of the mobilities of Po-210 generated ions in air, in the absence of TTIP vapor introduction are shown in Figure 3a. Data are reported in terms of ion concentration at the DMA outlet, assuming singly charged ions. Both positive and negative ions are monomodal, with the negative ion peak mobility at $Z_i^- = 1.88\ cm^2V^{-1}s^{-1}$ with a corresponding mobility diameter of 0.74 nm, and a positive ion peak mobility at $Z_i^+ = 1.43\ cm^2V^{-1}s^{-1}$ with a corresponding mobility diameter of 0.89 nm. In Figure 3b, we plot inverted distributions using equation (5), but neglected diffusion losses in tubing (because the ions are generated in the bipolar ion source) as well as the charge efficiency. Integrating this distributions yield positive and negative ion concentrations of 6.47 x 10^{10} m^{-3} and 3.14 x 10^{10} m^{-3}, respectively, hence the choice to use an ion concentration of 4.81 x 10^{10} m^{-3} in charge distribution calculations.

In calculating charge distributions, we neglect nanocluster concentration influences and treat ion concentrations for both polarities as constant and equal to one another, although we subsequently show this assumption is violated as nanocluster concentrations are likely similar in magnitude or greater than ion concentrations. We also further neglect differential losses of positive and negative ions in the bipolar charger (which likely leads to the lower observed

negative ion concentrations than positive) as well as heterogeneity in ion mobilities and masses, effects which are discussed in detail elsewhere (Hoppel & Frick, 1990; de La Verpilliere *et al.*, 2015; Carsí & Alonso, 2020; Ibarra *et al.*, 2020). Despite the inaccuracies introduced by making these assumptions, they drastically simplify charge distribution estimation (including the ability to neglect ion-ion recombination), enabling conversion of measured concentrations to nanocluster size distribution functions. It is likely that the inaccuracies introduced by the charge distribution calculation approach employed predominantly affect the absolutely values of the inferred size distributions, but have a lessened influence on the relative intensities of peaks in size distributions with respect to one another. Furthermore, accounting for ion depletion, as well as additional nanocluster collisional growth in sampling lines and the bipolar ion source, would require use of a detailed population balance model, tracking nanocluster size and charge distribution evolution. Such models are not trivial to accurately construct, and for the size range of interest further would require an estimate of the influence of potential interactions on nanocluster-nanocluster coagulation rates (Goudeli *et al.*, 2020).

Estimates of the bipolar ionization source dimensions yield a residence time in the ionization zone of 0.57 s. Using this residence time, the measured peak ion mobilities, calculated ion masses with equation (3), and estimated ion concentrations, the bipolar charge distribution calculated is provided in Figure 4a for 0.57 s residence in the bipolar ion source. As is universally the case in atmospheric pressure ionization with bipolar ions of similar mass and mobilities, the fraction of charged particles is extremely low (below 1%) in the nanocluster size range but increases with increasing nanocluster diameter. The expected higher fraction of negatively charged nanoclusters is the result of inputting higher electrical mobilities and lower masses for negative ions than for positive ions. As evidenced in Figure 4b, for constant assumed

ion concentration, the residence time appears to be insufficient time for nanoclusters to achieve a steady-state charge distribution, and overall ion characterization and charge distribution calculation confirms that while charge distributions for mobility measurement inversion can be calculated in the nanocluster size range, standard practices in mobility based size distribution inversion need to be substantially modified for this size range, and should be improved in the future to enable more quantitative measurements.

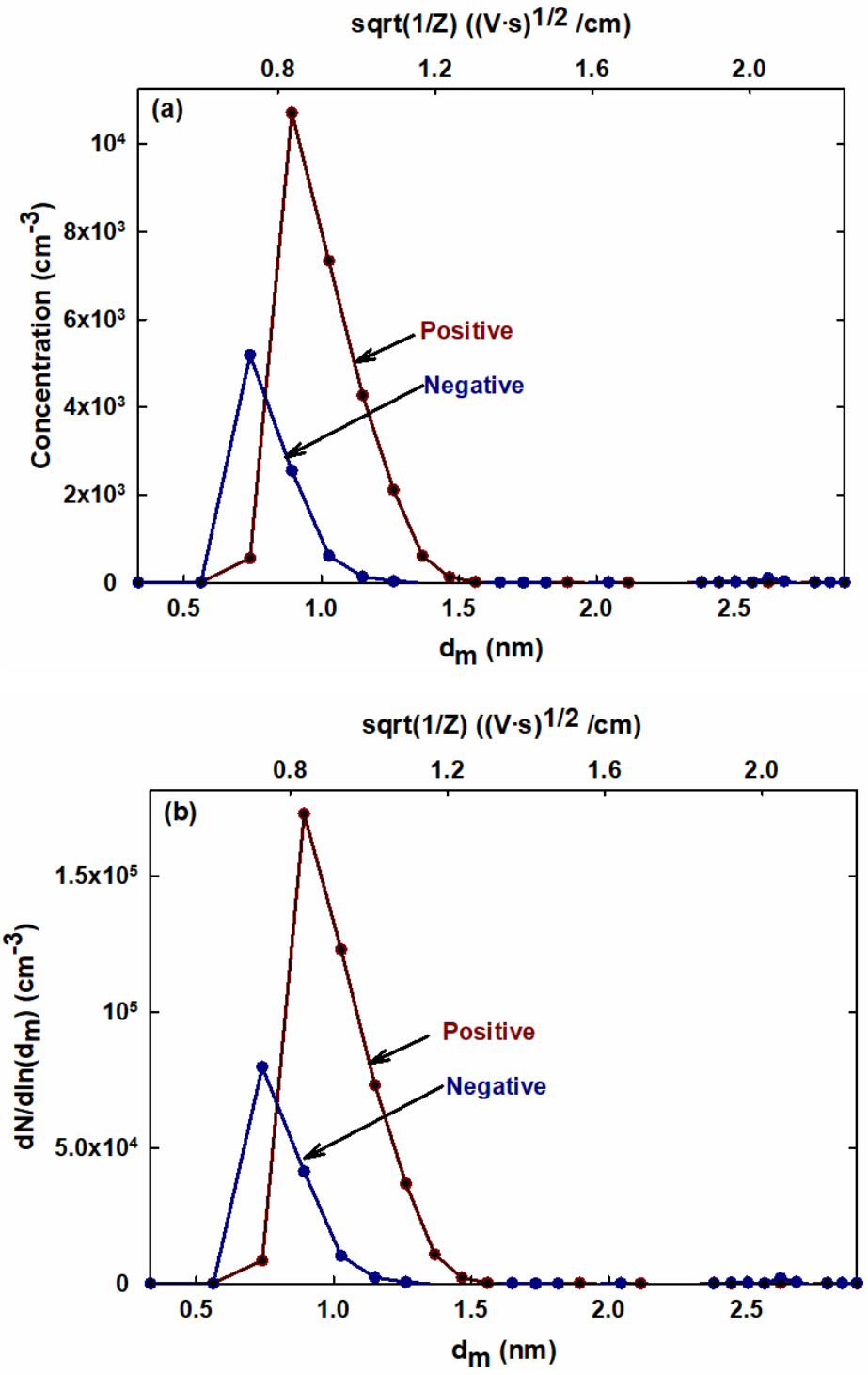

Figure 3. Measured ion inverse square-root of the mobility and mobility diameter spectra in terms of ion concentration at the DMA outlet for positive and negative Po-210 source-generated ions in air (a). Inverted ion size distributions accounting for the DMA transfer function in equation (5), but without any charge distribution correcting or tubing losses considered **(b)**.

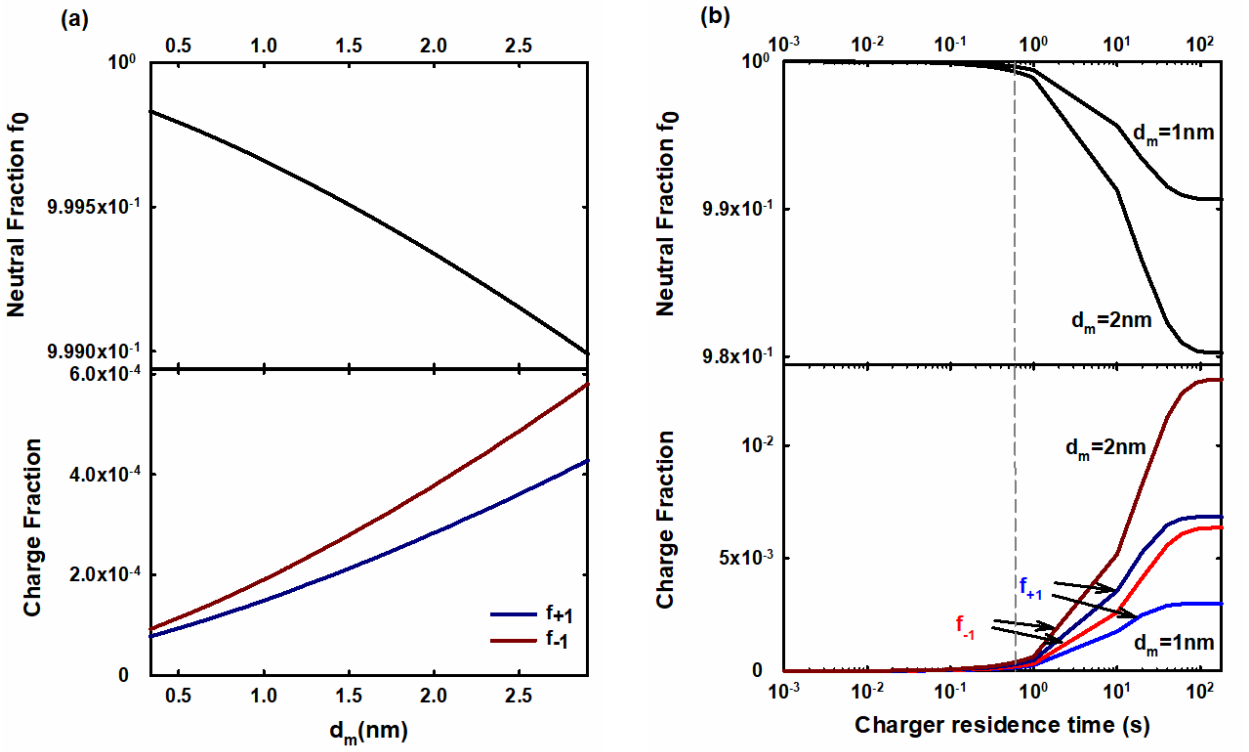

Figure 4. The neutral and charged nanocluster fractions for a residence time of 0.57 s **(a)** as well as the neutral and charged fractions as functions of time for 1 nm and 2 nm diameter nanoclusters with 10 L min^{-1} flow rate **(b)**.

3.2. Nanocluster Concentration Measurements

Without inversion, the measured charged nanocluster concentrations for 10 L min^{-1} flow rate through the furnace with temperature settings of 350° C, 475° C, and 600° C are shown in Figure 5 for both positively and negatively charged nanoclusters. In general, we observe two classes of species detected. First, in all circumstances, narrow peaks in spectra are observed in the diameter range from 0.50 nm to 1.5 nm. At lower temperatures, in both the negative and positive modes, the locations of these peaks coincide with the peaks observed in the absence of TTIP, and they are hence attributable to small molecular mass, high mobility ions generated from air (which are usually derived from chemical impurities in atmospheric pressure systems (Maißer, et al., 2015)). However, at higher temperatures, peaks at larger mobility diameters

become evident (and at smaller mobility diameters, in selected instances), which, like the air ion peaks, differ in position between the negative and positive modes. This first set of mobility peaks, both from air ions and those at higher temperature, can be contrasted with the second type of species detected, which all fall into a broadly distributed peak in the > 1.0 nm range for most negative spectra and > 1.25 nm range for most positive spectra. The broadly distributed peak is similar in magnitude and position when comparing different charge states for the same TTIP injection rate and temperature. We hence attribute this larger, broader peak, to formation and growth of nanoclusters, composed of TiO_2, or possibly partially-oxidized organometallic molecules.

First examining the smaller, discrete location peaks in spectra, we denote the peak positions with vertical lines in Figure 5. While earlier efforts have detected such peaks and interpreted them as multimeric TiO_2 species (Fang, et al., 2014), the inferred diameters, step size between peaks, and the finding that different mobility species are detected in the positive and negative mode are not consistent with these ions being attributable to TiO_2 nanoclusters. Approximating nanoclusters as bulk density spheres, discounting the polarization correction, a 1.0 nm nanocluster would correspond to approximately $(TiO_2)_{17}$. Ionized TiO_2 monomers and dimers would appear nearly indistinguishable from one another with mobilities close to the polarization limit. We hence suggest that in line with suggested mechanisms of TiO_2 nanocluster formation, such the discrete ions detected result from intermediate decomposition of TTIP (Buerger, et al., 2015; Boje *et al.*, 2017; Buerger, et al., 2017), and may be particularly stable multimeric species formed via collisions of these intermediates; this is also suggested by previously DMA (Wang, et al., 2014; Wang, et al., 2015) and DMA-MS measurements (Wang *et al.*, 2017). At higher TTIP injection rates, such intermediates appear to be incorporated into

growing nanoclusters via surface growth, as they are more prominent in spectra at reduced injection rates, wherein the nanocluster "collision sink" is less pronounced (i.e. there are fewer nanoclusters available to deplete reactive intermediates via uptake). We remark that efforts were made to minimize any polymeric tubing within the measurement system, which has been shown previously to "out-gas" organic and siloxane species which act as a source of contamination in atmospheric pressure electrical mobility measurements (Maißer, et al., 2015), further increasing the likelihood that these peaks arises from intermediate decomposition products and not from the vaporization of any system components. It is also interesting that the appearance of the larger mobility diameter, narrowly distributed peaks coincides with the depletion of the air ion peak; as alluded to in the prior section this does draw into question the assumption of constant ion concentrations in charge distribution estimation, an effect which will need to be addressed in future work further refining nanocluster size distribution measurement methods.

The inversion approached utilized here, similar to those conventionally used in inverting size distributions, assumes charging efficiencies are not sensitive to nanocluster chemical compositions. However, the presence of distinct ions in the positive and negative mode at disparate mobilities from one another suggests that these ions arise from molecules or molecular clusters which are ionizable solely as either cations or anions. Therefore, while we apply data inversion across the entirety of collected mobility spectra, inversion is specifically intended for examination of the second, broad peak of nanoclusters attributable to nucleation and growth. Figure 6 displays inverted size distribution functions for variable furnace temperature settings (variable profiles) and TTIP precursor flow rates, all for system flow rates of 10 L min^{-1} through the tube furnace. Inverted distributions from positive and negative mode measurements are not in perfect coincidence with one another, as the spectra were collected at different times and with

slightly different precursor flow rates, due to fluctuations in the mass flow rate into the bubbler resulting from changes in liquid content and the pressure drop through the bubbler. Nonetheless, there does not appear to be any obvious bias towards the positive or negative polarities, i.e. inverted size distributions resulting from both polarities are similar in peak location and magnitude when similar TTIP precursor flow rates and furnace temperature settings are applied. This suggests the charge distribution calculation approach we apply largely corrects for the observed higher concentrations of negatively charged nanoclusters than positively charged nanoclusters, and that the asymmetry in the raw data is due to the higher mobilities and higher charging efficiency for negative ions than positive ions.

Both negative and positive size distributions consistently show that the nanocluster peak increases in both mode diameter and in concentration as precursor concentration is increased, which is generally expected in gas phase synthesis systems (Chen *et al.*, 2018; Chen *et al.*, 2020). This is quite simply attributable to a greater extent of nucleation (a larger number of nanoclusters formed), larger extents of surface growth, and with higher number concentrations, increased levels of coagulation. The extent of reaction and nanocluster growth further increases with increases in reactor temperature. This is presumably because of the influence of gas temperature on TTIP decomposition rates. Hard-sphere theories do suggest that collisional growth rates for nanoclusters scale with square root of the temperature. However, more recent molecular dynamics simulations (Yang *et al.*, 2018; Goudeli, et al., 2020) show that because short-range attractive interactions appreciably increase collisional growth rates beyond hard-sphere estimates, yet potential influences are diminished with increasing temperature, temperature only weakly effects collisional growth rates in most nanoparticle-laden aerosols. Overall, results are in line with current understanding of gas phase synthesis process from

organometallic precursors. Nonetheless, we believe this is important to have demonstrated via measurements in the nanocluster regime, as to our knowledge, the spectra reported here are the first instance wherein discrete ion peaks attributable to reactive intermediates from TTIP decomposition and a broad peak attributable to nanoclusters are detected in the same mobility spectra. Prior efforts have identified the smaller, discrete ion peaks (Fang, et al., 2014; Wang, et al., 2015; Wang, et al., 2017; Vazquez-Pufleau, et al., 2020), but did not enable monitoring of the TiO_2 nanocluster size distribution as it evolves in the 1.5 nm – 2.5 nm size range (though it appears peaks corresponding to reactive intermediates and nanoclusters were detected in Wang et al (2014)). Observations were likely possible here because of the larger transport flow rates used compared to prior furnace studies (Wang, et al., 2015), and the better control of temperature-time history in the reactor in comparison to prior efforts utilizing 2-D flames (Fang, et al., 2014; Wang, et al., 2017). Furthermore, as expanded upon in the supporting information, the larger transport flow rates utilized led to less than 1% (and near 0.5%) of the Ti atoms from the TTIP precursor incorporated into nanoclusters. This confirms that in spectra we capture the earliest stages of the nanocluster formation and growth process.

As shown in Figure 7, increasing the flow rate through the tube furnace, which simultaneously leads to dilution of the precursor TTIP, reduction of the residence time in the furnace, and reduced temperatures, yields reduced nanocluster growth, and higher relative signal for the discrete ion peaks in comparison to the larger nanocluster peak. At the highest flow rates and shortest furnace residence times, formation of nanoclusters appears to be almost completely suppressed, with the mobility spectra and inverted size distributions dominated by small ions peaks, i.e., the proposed precursors to nanoclusters. This is again consistent with the existing depiction of metal oxide nucleation from organometallic precursors in the gas phase, and with

calculations it suggests most of the organometallic precursor remains unreacted in the measurement system.

Although measurements do provide insight into metal oxide nanocluster nucleation and growth via the simultaneous detection of distinct precursor ions and a growing size distribution of nanoclusters, more work will be needed to better verify proposed reaction pathways for organometallic precursor decomposition and nanocluster nucleation and growth, i.e., the chemical composition of precursor ions needs to be more clearly defined. Efforts towards chemical identification along these lines were made in Wang et al (2017); however, the authors excluded the possibility of residual organic groups within ions, and in doing so, they used ion identifications which are not chemically possible (e.g. $Ti_2O_{11}^-$). However, the densities inferred for precursor ions in their work (1.75 g cm^{-3}) would be consistent with that expected for organometallic intermediates.

We also remark that because the broad nanocluster peak does not clearly extend to below ~1.2 nm in either the positive or negative modes, we do not have evidence that nanoclusters with fewer than ~10 molecules are formed; the nanocluster peak appears unambiguously only at larger diameters. This suggests that at least for the case of TTIP decomposition, nanocluster formation and growth may not be initiated at atmospheric pressure by sub-nanometer, purely TiO_2 nanoclusters. For comparison, to date, metal oxide and noble clusters composed of fewer than 10 molecules have been analyzed from low pressure laser vaporization sources (Zemski *et al.*, 2002; Wu *et al.*, 2017; Abdul Latif *et al.*, 2018) and spark discharge systems (Maisser *et al.*, 2015; Domaschke *et al.*, 2019; Maisser *et al.*, 2021), hence it is certainly possible to detect such species via mobility analysis and mass spectrometry.

4. Conclusions

We have utilized differential mobility analysis to examine the formation and growth of nanoclusters via the decomposition of TTIP in a flow tube reactor with tuned TTIP precursor concentrations, system flow rates and residence times, and temperature profiles. Results show clearly that TTIP decomposition yields two distinct types of products detectable in mobility spectra; ions of specific mobilities largely in the sub-nanometer size range, with different peak locations for cations and anions, and a broadly distributed peak falling in the 1.5 nm – 2.5 nm for most examined reactor conditions. We attribute the first set of peaks to reactive intermediates from the decomposition of TTIP, for which atmospheric pressure chemical ionization yields either cations or anions (but not both), while the broad peak is attributable to growing nanoclusters, which are of unclear chemical composition. The extent of nanocluster formation and growth increases with increasing precursor concentration, reactor temperature, and residence time, qualitatively consistent with the standard picture of metal oxide synthesis from organometallic precursors. By simultaneously detecting reactive intermediates and growing nanoclusters in a flow tube reactor for the first time, this work contributes to the growing body of literature examining metal and ceramic nanocluster nucleation and growth in spark discharge (Maisser, et al., 2015; Domaschke, et al., 2019), non-thermal plasma (Kumar, et al., 2014; Chen, et al., 2020), flame (Carbone, et al., 2016; Tang, et al., 2017; Sharma, et al., 2021), and flow tube systems (Wang, et al., 2015; Vazquez-Pufleau, et al., 2020). This work also points to the need to better link the appearance and subsequent decay of reactive intermediates and identification of the precise species involved in nucleation of TiO_2 nanoparticles and their surface growth. This will likely require further refinement of mobility spectrometry coupled to mass spectrometry, which has yielded limited information about organometallic precursor decomposition in prior

work (Wang, et al., 2017), but has not yet enabled unambiguous detection of metal oxide nanoclusters resulting from organometallic decomposition. Future studies will also benefit from the development of models which explicitly propose schemes not only for precursor decomposition to intermediate species, but for nanocluster nucleation (Buerger, et al., 2015; Buerger, et al., 2017) as well as surface growth reactions involving decomposition intermediates across a wide temperature range.

5. Acknowledgements

This work was supported by US National Science Foundation (NSF) Award Number 2038173. The authors also acknowledge Mr. Sai Ranjeet Narayanan for his help with the initial experiment setup.

6. Supporting Information

The mobility spectra of THAB electrospray-generated ions used in DMA calibration, determination of the DMA full width at half maximum, a summary of all reported experimental conditions, a description of nanocluster penetration through system tubing, a description of the nanocluster-ion collision kernels used in charge distribution evaluation, and calculation of the fraction of TTIP utilized expended in growth reactions are available online.

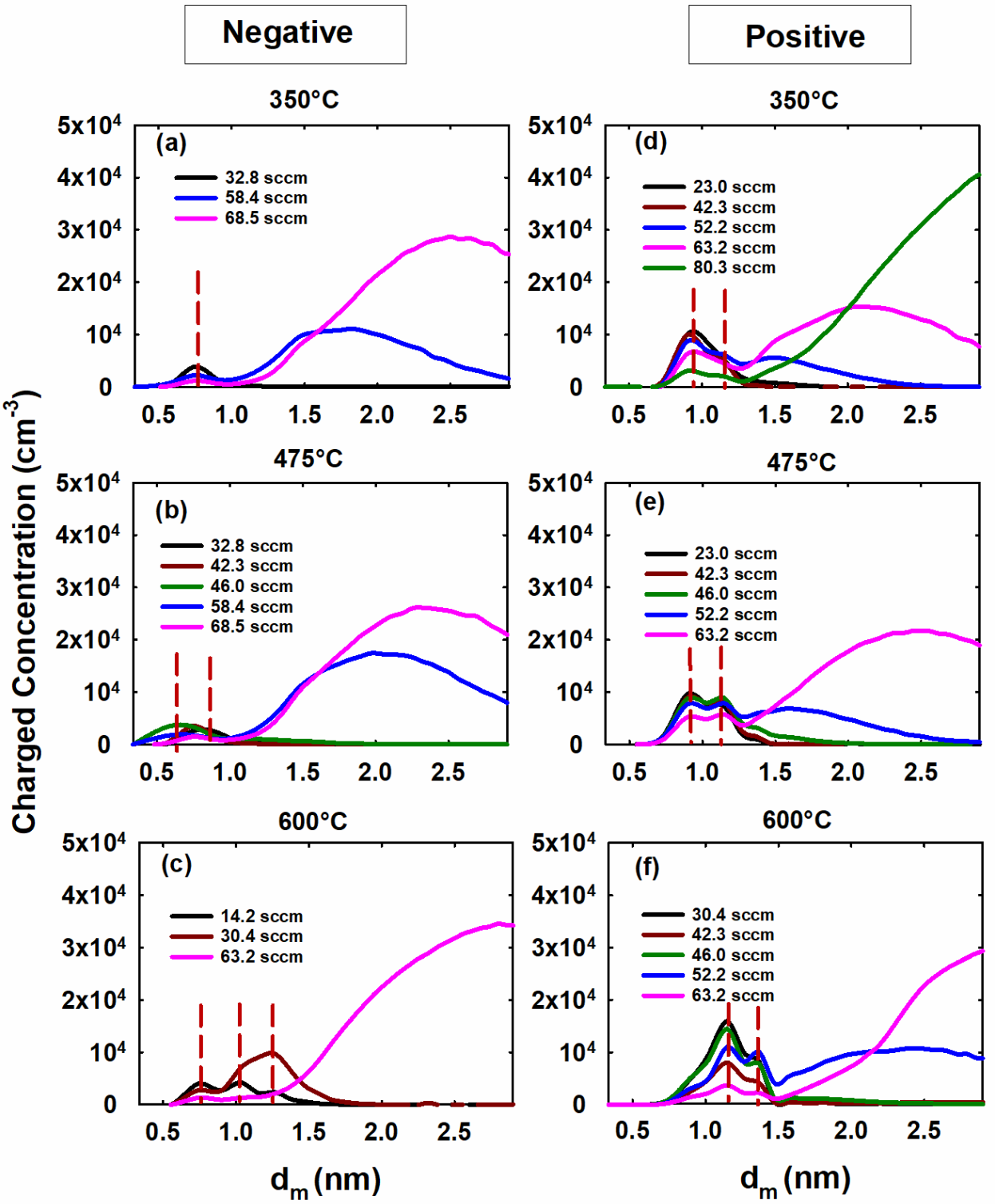

Figure 5. Measured nanocluster concentrations as a function of mobility diameter (based upon DMA peak voltage) for variable furnace temperature setting with 10 L min^{-1} flow rate. Saturated TTIP flow injection rates are provided in each sub-figure legend.

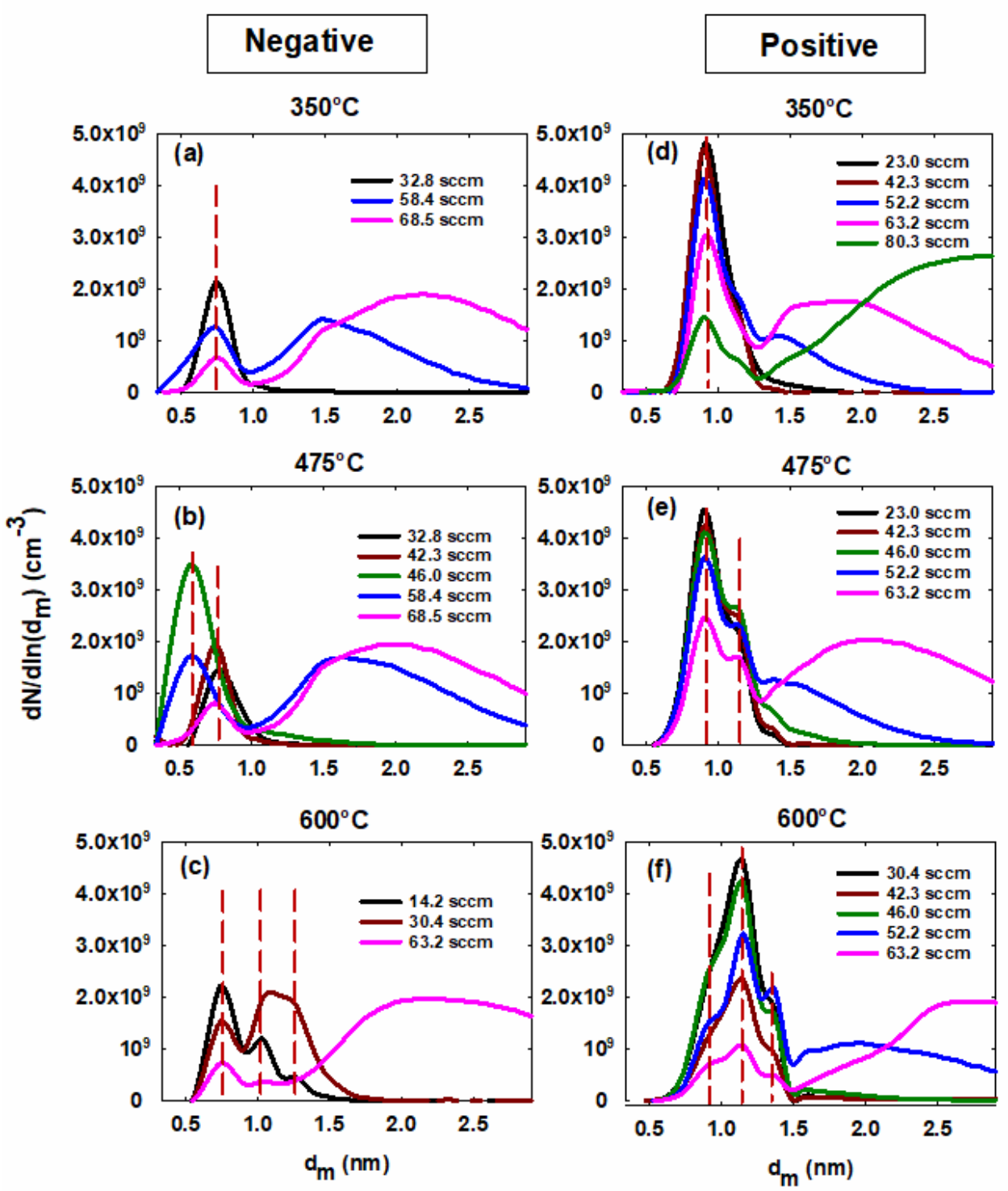

Figure 6. Nanocluster size distribution functions for variable furnace temperature setting with 10 L min^{-1} flow rate. Saturated TTIP flow injection rates are provided in each sub-figure legend.

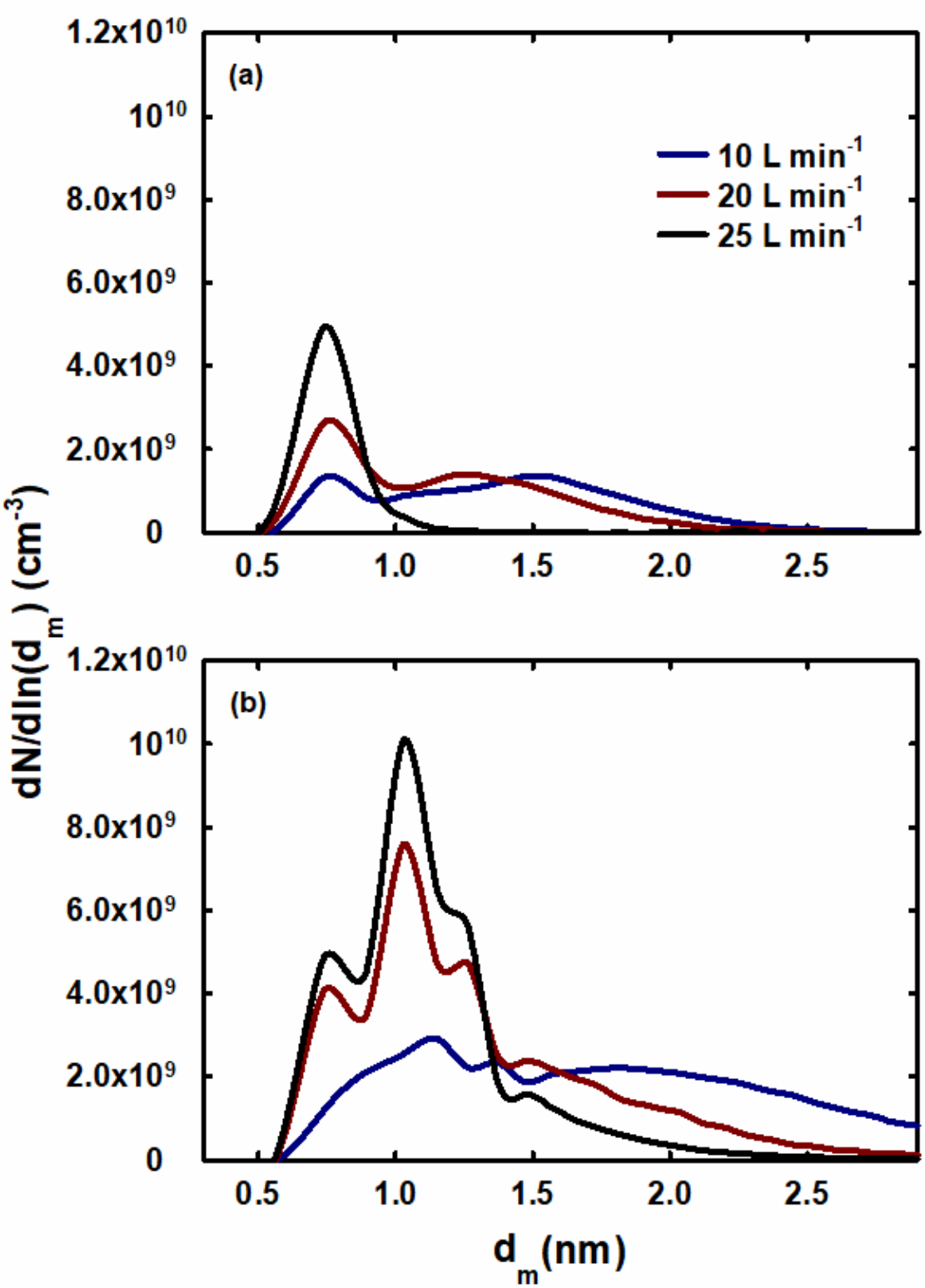

Figure 7. Nanocluster size distribution functions for variable furnace temperature setting with variable flow rate flow rate for both negative **(a)** and positive **(b)** charged nanoclusters. The nominal furnace temperature was 475^{o} C while the flow rate through the TTIP bubbler was 58.4 sccm.

References

Abdul Latif, M., Wu, J.W.J., Moriyama, R., Nakano, M., Ohshimo, K., & Misaizu, F. (2018). Stable Compositions and Structures of Copper Oxide Cluster Cations CunOm+ (n = 2–8) Studied by Ion Mobility Mass Spectrometry. *ACS Omega,* **3**, 18705-18713.

Adachi, M., Kousaka, Y., & Okuyama, K. (1985). Unipolar and bipolar diffusion charging of ultrafine aerosol particles. *Journal of Aerosol Science,* **16**, 109-123.

Boje, A., Akroyd, J., Sutcliffe, S., Edwards, J., & Kraft, M. (2017). Detailed population balance modelling of TiO2 synthesis in an industrial reactor. *Chemical Engineering Science,* **164**, 219-231.

Buerger, P., Nurkowski, D., Akroyd, J., & Kraft, M. (2017). A kinetic mechanism for the thermal decomposition of titanium tetraisopropoxide. *Proceedings of the Combustion Institute,* **36**, 1019-1027.

Buerger, P., Nurkowski, D., Akroyd, J., Mosbach, S., & Kraft, M. (2015). First-Principles Thermochemistry for the Thermal Decomposition of Titanium Tetraisopropoxide. *The Journal of Physical Chemistry A,* **119**, 8376-8387.

Carbone, F., Attoui, M., & Gomez, A. (2016). Challenges of measuring nascent soot in flames as evidenced by high-resolution differential mobility analysis. *Aerosol Science and Technology,* **50**, 740-757.

Carsí, M., & Alonso, M. (2020). A numerical study of bipolar charging and neutralization of ultrafine particles with uniformly generated heterogeneous ions. *Journal of Aerosol Science,* **149**, 105611.

Chen, X., Ghosh, S., Buckley, D.T., Sankaran, R.M., & Hogan, C.J. (2018). Characterization of the state of nanoparticle aggregation in non-equilibrium plasma synthesis systems. *Journal of Physics D: Applied Physics,* **51**, 335203.

Chen, X., Seto, T., Kortshagen, U.R., & Hogan, C.J. (2020). Size and structural characterization of Si nanocrystal aggregates from a low pressure nonthermal plasma reactor. *Powder Technology,* **373**, 164-173.

de La Verpilliere, J.L., Swanson, J.J., & Boies, A.M. (2015). Unsteady bipolar diffusion charging in aerosol neutralisers: A non-dimensional approach to predict charge distribution equilibrium behaviour. *Journal of Aerosol Science,* **86**, 55-68.

Dittus, F., & Boelter, L. (1985). Heat transfer in automobile radiators of the tubular type. *International communications in heat and mass transfer,* **12**, 3-22.

Domaschke, M., Lübbert, C., & Peukert, W. (2019). Analysis of ultrafine metal oxide particles in aerosols using mobility-resolved time-of-flight mass spectrometry. *Journal of Aerosol Science,* **137**, 105438.

Fang, J., Wang, Y., Attoui, M., Chadha, T.S., Ray, J.R., Wang, W.-N., Jun, Y.-S., & Biswas, P. (2014). Measurement of Sub-2 nm Clusters of Pristine and Composite Metal Oxides during Nanomaterial Synthesis in Flame Aerosol Reactors. *Analytical Chemistry,* **86**, 7523-7529.

Fernández-García, J., & Fernández de la Mora, J. (2013). Measuring the Effect of Ion-Induced Drift-Gas Polarization on the Electrical Mobilities of Multiply-Charged Ionic Liquid Nanodrops in Air. *Journal of the American Society for Mass Spectrometry,* **24**, 1872-1889.

Fernández de la Mora, J., & Kozlowski, J. (2013). Hand-held differential mobility analyzers of high resolution for 1–30 nm particles: Design and fabrication considerations. *Journal of Aerosol Science,* **57**, 45-53.

Fuchs, N.A. (1963). On the stationary charge distribution on aerosol particles in a bipolar ionic atmosphere. *Geofisica pura e applicata,* **56**, 185-193.

Girshick, S.L. (1997). Theory of nucleation from the gas phase by a sequence of reversible chemical reactions. *The Journal of Chemical Physics,* **107**, 1948-1952.

Gopalakrishnan, R., McMurry, P.H., & Hogan, C.J. (2015). The Bipolar Diffusion Charging of Nanoparticles: A Review and Development of Approaches for Non-Spherical Particles. *Aerosol Science and Technology,* **49**, 1181-1194.

Gopalakrishnan, R., Thajudeen, T., Ouyang, H., & Hogan, C.J. (2013). The unipolar diffusion charging of arbitrary shaped aerosol particles. *Journal of Aerosol Science,* **64**, 60-80.

Gormley, P.G., & Kennedy, M. (1948). Diffusion from a Stream Flowing through a Cylindrical Tube. *Proceedings of the Royal Irish Academy. Section A: Mathematical and Physical Sciences,* **52**, 163-169.

Goudeli, E., Lee, J., & Hogan, C.J. (2020). Silica nanocluster binding rate coefficients from molecular dynamics trajectory calculations. *Journal of Aerosol Science,* **146**, 105558.

Hoppel, W.A., & Frick, G.M. (1986). Ion—Aerosol Attachment Coefficients and the Steady-State Charge Distribution on Aerosols in a Bipolar Ion Environment. *Aerosol Science and Technology,* **5**, 1-21.

Hoppel, W.A., & Frick, G.M. (1990). The Nonequilibrium Character of the Aerosol Charge Distributions Produced by Neutralizes. *Aerosol Science and Technology,* **12**, 471-496.

Husmann, E., Thimsen, E., & Chen, X. (2021). Particle charge distributions in the effluent of a flow-through atmospheric pressure low temperature plasma. *Plasma Sources Science and Technology,* **30**, 075030.

Ibarra, I., Rodríguez-Maroto, J., & Alonso, M. (2020). Bipolar charging and neutralization of particles below 10 nm, the conditions to reach the stationary charge distribution, and the effect of a non-stationary charge distribution on particle sizing. *Journal of Aerosol Science,* **140**, 105479.

Jiang, J., Chen, D.-R., & Biswas, P. (2007). Synthesis of nanoparticles in a flame aerosol reactor with independent and strict control of their size, crystal phase and morphology. *Nanotechnology,* **18**, 285603.

Kangasluoma, J., Cai, R., Jiang, J., Deng, C., Stolzenburg, D., Ahonen, L.R., Chan, T., Fu, Y., Kim, C., Laurila, T.M., Zhou, Y., Dada, L., Sulo, J., Flagan, R.C., Kulmala, M., Petäjä, T., & Lehtipalo, K. (2020). Overview of measurements and current instrumentation for 1–10 nm aerosol particle number size distributions. *Journal of Aerosol Science,* **148**, 105584.

Kim, M., Osone, S., Kim, T., Higashi, H., & Seto, T. (2017). Synthesis of nanoparticles by laser ablation: A review. *KONA Powder and Particle Journal*, 2017009.

Knutson, E.O., & Whitby, K.T. (1975). Aerosol classification by electric mobility: apparatus, theory, and applications. *Journal of Aerosol Science,* **6**, 443-451.

Kortshagen, U.R., Sankaran, R.M., Pereira, R.N., Girshick, S.L., Wu, J.J., & Aydil, E.S. (2016). Nonthermal Plasma Synthesis of Nanocrystals: Fundamental Principles, Materials, and Applications. *Chemical Reviews,* **116**, 11061-11127.

Kumar, A., Kang, S., Larriba-Andaluz, C., Ouyang, H., Hogan, C.J., & Sankaran, R.M. (2014). Ligand-free Ni nanocluster formation at atmospheric pressure via rapid quenching in a microplasma process. *Nanotechnology,* **25**, 385601.

Larriba-Andaluz, C., & Carbone, F. (2021). The size-mobility relationship of ions, aerosols, and other charged particle matter. *Journal of Aerosol Science,* **151**, 105659.

Larriba, C., & Hogan, C.J. (2013a). Free molecular collision cross section calculation methods for nanoparticles and complex ions with energy accommodation. *Journal of Computational Physics,* **251**, 344-363.

Larriba, C., & Hogan, C.J. (2013b). Ion Mobilities in Diatomic Gases: Measurement versus Prediction with Non-Specular Scattering Models. *The Journal of Physical Chemistry A,* **117**, 3887-3901.

Li, L., Chahl, H.S., & Gopalakrishnan, R. (2020). Comparison of the predictions of Langevin Dynamics-based diffusion charging collision kernel models with canonical experiments. *Journal of Aerosol Science,* **140**, 105481.

Li, L., & Gopalakrishnan, R. (2021). An experimentally validated model of diffusion charging of arbitrary shaped aerosol particles. *Journal of Aerosol Science,* **151**, 105678.

Lindberg, C.S., Manuputty, M.Y., Buerger, P., Akroyd, J., & Kraft, M. (2019). Numerical simulation and parametric sensitivity study of titanium dioxide particles synthesised in a stagnation flame. *Journal of Aerosol Science,* **138**, 105451.

Maisser, A., Barmpounis, K., Attoui, M.B., Biskos, G., & Schmidt-Ott, A. (2015). Atomic Cluster Generation with an Atmospheric Pressure Spark Discharge Generator. *Aerosol Science and Technology,* **49**, 886-894.

Maisser, A., Barmpounis, K., Holm, S., Attoui, M., Schmidt-Ott, A., Kangasluoma, J., & Biskos, G. (2021). Characterization of atmospheric-pressure spark generated atomic silver and gold clusters by time-of-flight mass spectrometry. *Journal of Aerosol Science,* **156**, 105780.

Maißer, A., Thomas, J.M., Larriba-Andaluz, C., He, S., & Hogan, C.J. (2015). The mass–mobility distributions of ions produced by a Po-210 source in air. *Journal of Aerosol Science,* **90**, 36-50.

Mäkelä, J.M., Jokinen, V., Mattila, T., Ukkonen, A., & Keskinen, J. (1996). Mobility distribution of acetone cluster ions. *Journal of Aerosol Science,* **27**, 175-190.

Mangolini, L. (2017). Monitoring non-thermal plasma processes for nanoparticle synthesis. *Journal of Physics D: Applied Physics,* **50**, 373003.

Marlow, W.H., & Brock, J.R. (1975). Calculations of bipolar charging of aerosols. *Journal of Colloid and Interface Science,* **51**, 23-31.

Meierhofer, F., & Fritsching, U. (2021). Synthesis of Metal Oxide Nanoparticles in Flame Sprays: Review on Process Technology, Modeling, and Diagnostics. *Energy & Fuels,* **35**, 5495-5537.

Meuller, B.O., Messing, M.E., Engberg, D.L.J., Jansson, A.M., Johansson, L.I.M., Norlén, S.M., Tureson, N., & Deppert, K. (2012). Review of Spark Discharge Generators for Production of Nanoparticle Aerosols. *Aerosol Science and Technology,* **46**, 1256-1270.

Němec, T., Šonský, J., Gruber, J., de Prado, E., Kupčík, J., & Klementová, M. (2020). Platinum and platinum oxide nanoparticles generated by unipolar spark discharge. *Journal of Aerosol Science,* **141**, 105502.

Ouyang, H., Gopalakrishnan, R., & Hogan, C.J. (2012). Nanoparticle collisions in the gas phase in the presence of singular contact potentials. *The Journal of Chemical Physics,* **137**, 064316.

Schulz, C., Dreier, T., Fikri, M., & Wiggers, H. (2019). Gas-phase synthesis of functional nanomaterials: Challenges to kinetics, diagnostics, and process development. *Proceedings of the Combustion Institute,* **37**, 83-108.

Sharma, G., Dhawan, S., Reed, N., Chakrabarty, R., & Biswas, P. (2019). Collisional growth rate and correction factor for TiO2 nanoparticles at high temperatures in free molecular regime. *Journal of Aerosol Science,* **127**, 27-37.

Sharma, G., Wang, M., Attoui, M., You, X., & Biswas, P. (2021). Measurement of sub-3 nm flame-generated particles using butanol CPCs in boosted conditions. *Aerosol Science and Technology,* **55**, 785-794.

Siefering, K.L., & Griffin, G.L. (1990). Growth Kinetics of CVD TiO2: Influence of Carrier Gas. *Journal of The Electrochemical Society,* **137**, 1206-1208.

Stolzenburg, M.R., & McMurry, P.H. (2008). Equations Governing Single and Tandem DMA Configurations and a New Lognormal Approximation to the Transfer Function. *Aerosol Science and Technology,* **42**, 421-432.

Suresh, V., Li, L., Redmond Go Felipe, J., & Gopalakrishnan, R. (2021). Modeling nanoparticle charge distribution in the afterglow of non-thermal plasmas and comparison with measurements. *Journal of Physics D: Applied Physics,* **54**, 275205.

Swihart, M.T. (2003). Vapor-phase synthesis of nanoparticles. *Current Opinion in Colloid & Interface Science,* **8**, 127-133.

Tang, Q., Cai, R., You, X., & Jiang, J. (2017). Nascent soot particle size distributions down to 1nm from a laminar premixed burner-stabilized stagnation ethylene flame. *Proceedings of the Combustion Institute,* **36**, 993-1000.

Ude, S., & de la Mora, J.F. (2005). Molecular monodisperse mobility and mass standards from electrosprays of tetra-alkyl ammonium halides. *Journal of Aerosol Science,* **36**, 1224-1237.

Vazquez-Pufleau, M., Wang, Y., Biswas, P., & Thimsen, E. (2020). Measurement of sub-2 nm stable clusters during silane pyrolysis in a furnace aerosol reactor. *The Journal of Chemical Physics,* **152**, 024304.

Wang, H. (2011). Formation of nascent soot and other condensed-phase materials in flames. *Proceedings of the Combustion Institute,* **33**, 41-67.

Wang, Y., Fang, J., Attoui, M., Chadha, T.S., Wang, W.-N., & Biswas, P. (2014). Application of Half Mini DMA for sub 2nm particle size distribution measurement in an electrospray and a flame aerosol reactor. *Journal of Aerosol Science,* **71**, 52-64.

Wang, Y., Kangasluoma, J., Attoui, M., Fang, J., Junninen, H., Kulmala, M., Petäjä, T., & Biswas, P. (2017). Observation of incipient particle formation during flame synthesis by tandem differential mobility analysis-mass spectrometry (DMA-MS). *Proceedings of the Combustion Institute,* **36**, 745-752.

Wang, Y., Liu, P., Fang, J., Wang, W.-N., & Biswas, P. (2015). Kinetics of sub-2 nm TiO2 particle formation in an aerosol reactor during thermal decomposition of titanium tetraisopropoxide. *Journal of Nanoparticle Research,* **17**, 147.

Wergen, L., Domaschke, M., Herre, P., Wu, M., Spiecker, E., & Peukert, W. (2019). Aerosol synthesis of germanium nanoparticles supported by external seeding: Theoretical and experimental analysis. *Journal of Aerosol Science,* **128**, 50-61.

Wiedensohler, A. (1988). An Approximation of the Bipolar Charge-Distribution for Particles in the Sub-Micron Size Range. *Journal of Aerosol Science,* **19**, 387-389.

Wu, J.W.J., Moriyama, R., Nakano, M., Ohshimo, K., & Misaizu, F. (2017). Compositions and structures of niobium oxide cluster ions, NbmOn±, (m = 2–12), revealed by ion mobility mass spectrometry. *Physical Chemistry Chemical Physics,* **19**, 24903-24914.

Yang, H., Goudeli, E., & Hogan, C.J. (2018). Condensation and dissociation rates for gas phase metal clusters from molecular dynamics trajectory calculations. *The Journal of Chemical Physics,* **148**, 164304.

Zemski, K.A., Justes, D.R., & Castleman, A.W. (2002). Studies of Metal Oxide Clusters: Elucidating Reactive Sites Responsible for the Activity of Transition Metal Oxide Catalysts. *The Journal of Physical Chemistry B,* **106**, 6136-6148.